PHILOSOPHICAL MAGAZINE A, 1982, VOL. 46, NO. 5, 737–759

A model for the effect of grain size on the yield stress of metals

By MARC A. MEYERS
Department of Metallurgical and Materials Engineering, New Mexico Institute of Mining and Technology, Socorro, New Mexico 87801, U.S.A.

and E. ASHWORTH
Department of Mining Engineering, South Dakota School of Mines and Technology, Rapid City, South Dakota 57701, U.S.A.

[Received 7 January 1982 and accepted 30 April 1982]

ABSTRACT

It is proposed that the grain-size dependence of the yield stress of metals is due to the elastic incompatibility stresses at the grain boundaries. For clarity, the process of yielding is divided into three stages. In the *first stage* (prior to microyielding), the differences in elastic properties arising from the elastic anisotropy of adjacent grains establish localized stress concentrations at the grain boundaries. In the *second stage*, the stress concentrations at the grain boundaries result in localized plastic flow; this is the microyield region. The generation and motion of these 'geometrically necessary' dislocations attenuates the stress concentrations; a work-hardened grain-boundary layer is formed. As the stress is increased, the polycrystalline metal acts as a composite material consisting of a continuous network of a work-hardened grain-boundary material and discontinuous bulk material. The bulk is prevented from flowing plastically because the continuous network of work-hardened grain-boundary film acts as a reinforcement. Macroyielding occurs when the applied stress is such that the grain-boundary film reaches its flow stress level; this is the *third stage*. Qualitatively, a polycrystal with a greater grain size has a proportionately smaller amount of grain-boundary reinforcement network and, consequently, a lower macroyield stress. This concept is developed into quantitative relationships between the grain diameter and the macroyield stress. Finite-element analysis is used to establish the value of the grain-boundary stresses caused by elastic compatibility conditions for a few simple cases. Theoretical predictions are compared with experimental observations made for nickel over a wide range of grain sizes.

§ 1. INTRODUCTION

The well-known Hall–Petch relationship (Hall 1951, Petch 1953) has been applied to a variety of different metals over the past 20 years with considerable success. A number of theories explaining the effect in terms of dislocation–grain-boundary interactions have been advanced. The first generation of theories (Hall 1951, Petch 1953, Cottrell 1958) is based on the idea of pile-up. The important concept of the grain boundary as a dislocation source was introduced by Mott (1946) and later by Li (1962, 1963 a); Li proposed a Hall–Petch-type relationship (Li 1963 *b*, Li and Chou 1970) based on grain-boundary ledges acting as dislocation sources. The Hall–Petch relationship is not free

0141-8610/82/4605 0737 $03·00

of controversy (Baldwin 1958, Conrad 1963); systematic experimental investigations for Armco iron (Anderson, King and Spreadborough 1968), modified AISI 1010 steel (Abrahamsom 1968) and nickel (Thompson 1975, 1977) over a broad range of grain sizes (4–200 μm for Armco iron; 0·34–10 μm for AISI 1010; 0·12–130 μm for nickel) showed very clearly that the plot of yield stress versus $D^{-1/2}$ is not linear. These results indicate that the linear behaviour is an approximation applicable only over a limited range of grain sizes.

Experimental evidence obtained by transmission electron microscopy indicating that grain boundaries are sources of dislocations (Tangri and Malis 1972, Murr 1975, Murr and Hecker 1979) has steadily been amassing, and recent observations confirm the fact that the onset of macroyielding is associated with dislocation generation from grain-boundary sources (Murr and Hecker 1979). Additionally, Sethi and Gibala (1976, 1977) have shown conclusively that dislocations generated at an interface between a single crystal and an oxide layer played an important role in the low-temperature macroyield stress.

However, the initiation of plastic flow takes place at stresses much lower than the conventional macroyield stress. Thus, the name microyield stress is commonly used to designate the stress at which the first indications of dislocation activity are noticeable, while macrostress is characterized by massive dislocation generation and motion, and a substantial deviation from the elastic deformation regime. There is a remarkable group (in their self-consistency) of papers devoted to microyielding in the Fe–3% Si alloy and its study by etch-pitting techniques. Suits and Chalmers (1961), Worthington and Smith (1964), Brentnall and Rostoker (1965) and Douthwaite and Evans (1973) all presented evidence that is mutually supportive: the microstrain region is characterized by dislocation emission from grain boundaries, these being the main sources. The critical experiment conducted by Douthwaite and Evans (1973) showed incontrovertibly that the stresses are higher in the grain-boundary region than in the centre of the grains. They made a scratch on the surface of a specimen, subsequently pulling it in tension. Dislocation emission from the grain boundaries started at a stress below that at which the dislocations generated by the scratch could move. This proves that the stress at the grain boundaries was higher than that at the scratch (representative of the bulk). Margolin and Stanescu (1975) found similar results for β-titanium: they report the onset of plastic deformation at the grain boundaries, proceeding inwards; based on their observations they proposed an expression for polycrystalline strengthening at constant strain as a function of grain size. The model proposed here is an extension and generalization of this.

The stress required for twinning provides additional support for the hypothesis of higher stresses at grain boundaries. At lower temperatures, b.c.c. metals exhibit a marked decrease in the mobility of screw dislocations (Talia, Fernandez, Sethi and Gibala 1980) rendering twinning a more attractive deformation mechanism. Hull (1961) found, for Fe–3% Si, that a Hall–Petch-type relationship was obeyed when yielding was initiated by twinning; similar results were found by Marcinkowski and Lipsitt (1962) for chromium.

The experimental evidence presented in the above references, among other sources, and the concepts of inhomogeneous plastic flow developed by Ashby (1970, 1971), Thompson and co-workers (Thompson, Baskes and Flanagan 1973, Thompson 1975, 1977) and Margolin and co-workers (Margolin and

Stanescu 1975, Jinoch, Ankem and Margolin 1978, Ankem and Margolin 1980) clearly show that the early theories of the effect of grain size on the yield stress are not realistic. The object of this paper is to propose a model consistent with the experimental observations above and incorporating the concept of inhomogeneous elastic and plastic deformation. The model is divided, for the sake of clarity, into three different stages. These stages are characterized by the dominance of different deformation modes and stress distributions.

First stage. The difference in elastic response between adjacent grains is responsible for the generation of incompatibility stresses at the grain boundaries (fig. 1 (*a*)). These incompatibility stresses, added to the resolved shear stress due to the applied load, result in a total stress at the grain boundaries considerably higher than that experienced by the bulk of the grain ($\sigma_{GB} > \sigma_B$). Hence, the grain boundary flows plastically prior to the bulk (fig. 1 (*b*)).

Fig. 1

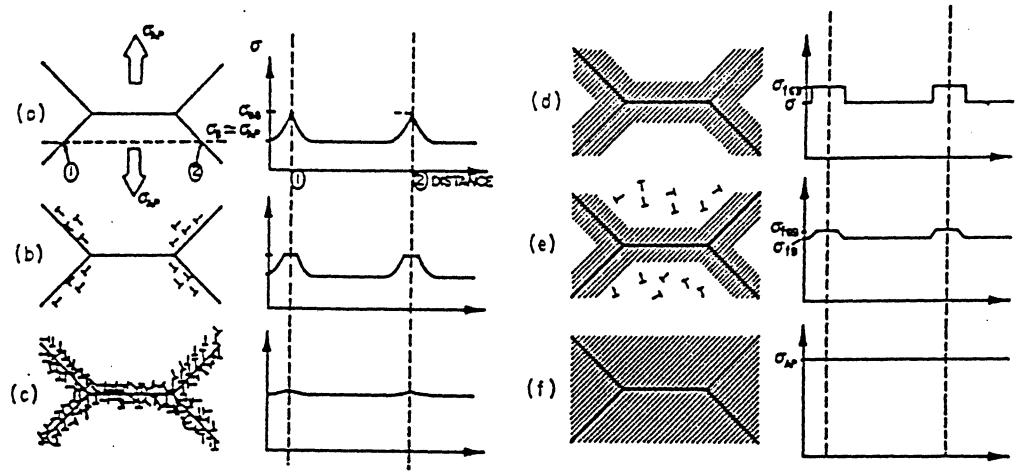

Sequence of stages in polycrystalline deformation, starting with (*a*, *b*) localized plastic flow in the grain-boundary regions (microyielding), forming a grain-boundary work-hardened layer (*c*, *d*) that effectively reinforces the microstructure, and leading to (*e*, *f*) macroyielding in which the bulk of the grains undergo plastic deformation.

Second stage. The plastic flow of the grain-boundary region attenuates the stress concentration ; geometrically necessary dislocations accommodate these stresses (figs. 1 (*b*) and 1 (*c*)). This marks the onset of microyielding. The dislocations do not propagate throughout the whole grain because of cross-slip induced by the difference of orientation between the maximum shear stress (due to the applied load) and the stress concentration caused by elastic incompatibility. The work-hardened grain-boundary layer has a flow stress σ_{iGB}, while the bulk has a flow stress σ_{iB} ($\sigma_{iGB} > \sigma_{iB}$). The material behaves, at increasing applied loads, as a composite made out of a continuous network of grain-boundary film with flow stress σ_{iGB} and of discontinuous ' islands ' of bulk material with flow stress σ_{iB}. The increasing applied stress σ_{AP} does not produce plastic flow in the bulk, in spite of the fact that $\sigma_{AP} > \sigma_{iB}$, because the continuous grain-boundary network provides the structure with rigidity

(fig. 1 (*d*)). The total strain in the continuous grain-boundary network does not exceed 0·005, since it is elastic; hence, plastic deformation in the bulk is inhibited. This situation can be termed plastic incompatibility.

Third stage. When the applied load is such that the stress in the grain boundary region becomes equal to σ_{IGB}, plastic deformation re-establishes itself in this region. The plastic deformation of the continuous matrix results in increases in stress in the bulk with plastic flow (fig. 1 (*c*)). This marks the onset of *macroyielding*. After a certain amount of plastic flow, dislocation densities in the bulk and grain-boundary regions become the same; since both regions have the same flow stress, plastic incompatibility disappears, and one has $\sigma_{AP}=\sigma_{GB}=\sigma_B$ (fig. 1 (*f*)).

The nature and extent of the elastic incompatibility stresses will be discussed and calculated in § 2; finite-element analysis is used to establish quantitatively their magnitude. Section 3 contains the derivation of the model leading to equations relating the macroyield stress to the grain diameter; predictions of the model are compared with experimental observations reported by Thompson (1977) in § 4.

§ 2. Elastic incompatibility

2.1. *Basic assumptions*

Although a polycrystalline aggregate is isotropic if the grains are randomly oriented, the individual grains exhibit the elastic anisotropy characteristic of their crystal symmetry. Hook and Hirth (1967) have investigated in detail the compatibility stresses using bicrystals. The approach used here is similar. A few simplifying assumptions are required. Although Smith (1952) has shown that grains in an ideal polycrystal are tetrakaidecahedra, two cubic and adjacent crystals will be considered and the interfacial stresses will be determined as a function of applied stresses. It is known that there are long-range interactions between grains: for simplicity, they will be neglected. An important assumption used is that the *stress* acting on all the grains is the same. The assumption made in the analyses of both Taylor (1938) and Bishop and Hill (1951) of the plastic deformation of polycrystalline aggregates is that all individual grains undergo the same *strain* as the tensile specimen. This assumption is not applicable here, as will be shown by the following analogy. The grains can be imagined as rubber and steel spheres filling a box. If a ram compresses the top of the box, the rubber spheres will undergo more deformation than the steel spheres. The Taylor–Bishop–Hill analysis is realistic in the plastic regime (constant volume, $\nu=0{\cdot}5$), while the assumption of the present model parallels more closely the elastic response of metals ($\nu\simeq 0{\cdot}3$). The Taylor–Bishop–Hill analysis is unable to predict a grain-size dependence of yield stress and work hardening. Recently, the effect of grain size on work hardening has been incorporated by Thompson by applying and modifying the concepts of Ashby (1970, 1971) on inhomogeneous deformation; however, this treatment is restricted to the plastic regime.

Hirth (1972) divided the incompatibility effects into two types. This same approach will be used here, and a longitudinal and a shear incompatibility will be treated. Figure 2 (*a*) shows two cubic grains: when subjected to the

Fig. 2

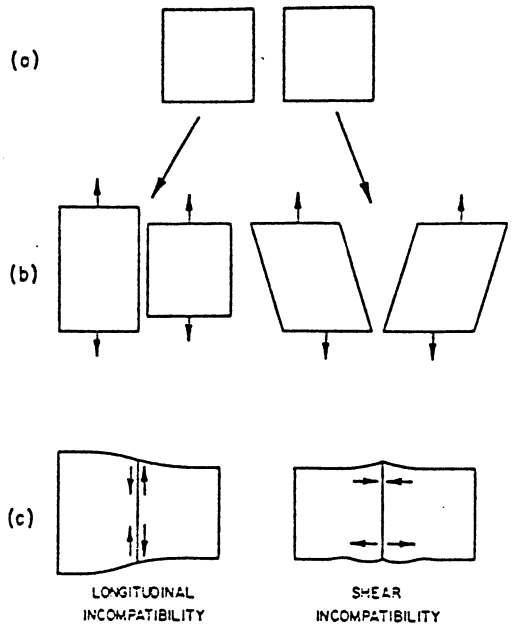

Development of incompatibility stresses along interface between two grains. (*a*) Initial cubic grains with identical dimensions. (*b*) Deformation of two grains under identical applied stresses. (*c*) Incompatibility stresses developed at interfaces.

same applied stress σ_{AP}, they will exhibit different strains if their crystallographic orientation is different. Figure 2 (*b*) shows how these distortions might take place. The interfacial bonding, however, establishes the condition of continuity of strains across the grain boundary ; fig. 2 (*c*) shows this situation. The left-hand side of the figure shows the longitudinal incompatibility, in which the crystallographic orientation is such that the faces of the cube remain perpendicular to each other. Crystallographic orientations such as [100] and [111] are characterized by this type of response. The right-hand side of fig. 2 (*c*) shows the situation in which the applied stress σ_{AP} generates shear strains in the reference system defined by the tensile axis. This occurs for orientations such as [110] ; it is called, in this paper, shear incompatibility. The longitudinal and shear incompatibilities will be assessed in §§ 2.2 and 2.3.

2.2. *Longitudinal incompatibility*

In order to determine the elastic longitudinal strain undergone by the monocrystalline cubes, it is convenient to convert the elastic constants into an effective elastic modulus. The determination of Young's modulus of single crystals is described by Nye (1957). For crystal systems exhibiting cubic symmetry,

$$\frac{1}{E_{ijk}} = S_{11} - 2(S_{11} - S_{12} - \tfrac{1}{2}S_{44})(l_i^2\, l_j^2 + l_j^2\, l_k^2 + l_i^2\, l_k^2), \qquad (1)$$

where E_{ijk} is Young's modulus along the $[ijk]$ direction, S_{11}, S_{12} and S_{44} are the compliances of the crystal and l_i, l_j and l_k are the direction cosines of

Compliance constants, Poisson's ratios and elastic moduli along [100], [110] and [111] for iron and nickel (McGregor Tegart 1966).

Elastic constant (ambient temperature)	Metal	
	Fe	Ni
$S_{11}(\text{Pa}^{-1})$	$0{\cdot}76\times10^{-11}$	$0{\cdot}73\times10^{-11}$
$S_{12}(\text{Pa}^{-1})$	$-0{\cdot}287\times10^{-11}$	$-0{\cdot}27\times10^{-11}$
$S_{44}(\text{Pa}^{-1})$	$0{\cdot}892\times10^{-11}$	$0{\cdot}80\times10^{-11}$
ν	0·28	0·31
l_i, l_j, l_k[100]	1, 0, 0	1, 0, 0
l_i, l_j, l_k[110]	$\frac{\sqrt{2}}{2}\ \frac{\sqrt{2}}{2}\ 0$	$\frac{\sqrt{2}}{2}\ \frac{\sqrt{2}}{2}\ 0$
l_i, l_j, l_k[111]	$\frac{\sqrt{3}}{3}\ \frac{\sqrt{3}}{3}\ \frac{\sqrt{3}}{3}$	$\frac{\sqrt{3}}{3}\ \frac{\sqrt{3}}{3}\ \frac{\sqrt{3}}{3}$
$E_{[100]}$(GPa)	125·0	136·9
$E_{[110]}$(GPa)	200·0	232·5
$E_{[111]}$(GPa)	272·7	303·0

Fig. 3

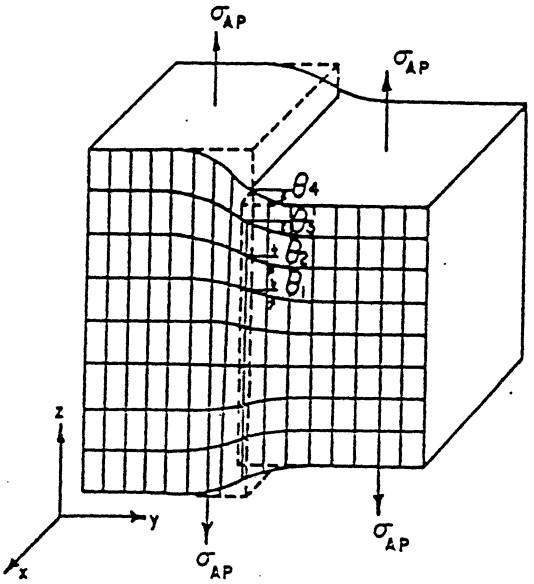

Deformation of two cubic grains showing longitudinal elastic incompatibility (for instance [111] on right and [100] on left). Compatibility restrictions producing distortions $\theta_1 < \theta_2 < \theta_3 < \theta_4$ (and associated shear strains) at interface.

the [ijk] direction with respect to the crystal axes. For the cubic-system the [100], [110] and [111] directions provide the extremes of response. The table lists the compliance constants and direction cosines of the [100], [110] and [111] directions for iron and nickel; from these the elastic moduli are calculated by applying eqn. (1). It can be seen from the table that the differences in elastic moduli are dramatic. Young's modulus in the [111] direction is over twice as high as in the [100] direction; this is the single most important fact in the derivation.

The [100] grain would undergo roughly twice the strain of [111] (fig. 2 (b)). However, they are bonded, and the compatibility conditions cause considerable distortion at the interface (fig. 3). An imaginary grid drawn on the face of the cubes shows the distortions. One can see clearly that the angle θ increases as one moves away from the centre plane ($\theta_4 > \theta_3 > \theta_2 > \theta_1 > \theta_0 = 0$). The distortion θ generates the interfacial shear stresses. The total shear stress (and strain) acting on the interface are the tensorial sums of two components (sum of components referred to same system of axes): the homogeneous shear component of the applied tensile stress (and strain) and the localized interfacial shear stress (and strain) due to anisotropy. Thus,

$$\tau_T = \tau_I + \tau_H \tag{2}$$

or

$$\gamma_T = \gamma_I + \gamma_H, \tag{3}$$

where the indices T, I and H refer to the total, interfacial and homogeneous stresses and strains. In order to obtain this total stress, use will be made of the principle of superposition which states that two strains may be combined by direct superposition. The interfacial strains have to be calculated as functions of the angle between the interface (grain boundary) and the tensile axis. Figure 4 shows the configuration for $\alpha = 90°$, $\alpha = 0$ and $0 < \alpha < 90°$. The calculation of interfacial strains is given in the Appendix, using the finite-element method for two geometries: $\alpha = 0$ and $\alpha = 90°$. The finite-element method has to be introduced because it is exceedingly complicated to obtain the displacement profiles by conventional methods of analysis. For a general orientation of α, one can decompose the stresses as seen in fig. 4 (c). The superposition of the interfacial strains due to the four stress systems applied separately provides the overall interfacial strain, which is

$$\gamma_I = (\gamma_I)_1 + (\gamma_I)_2 + (\gamma_I)_3 + (\gamma_I)_4, \tag{4}$$

$(\gamma_I)_2$ being obtained from a stress geometry identical to that in fig. 3.

The shear strains $(\gamma_I)_1$ and $(\gamma_I)_2$ depend on the level of the externally applied load. It is shown in the Appendix that $(\gamma_I)_1$ is proportional to the applied stress σ_{AP}. For the general stress configuration of fig. 4 (c), one has

$$(\gamma_I)_1 = k_1 \sigma_{AP} \sin \alpha. \tag{5}$$

Similarly

$$(\gamma_I)_2 = k_2 \sigma_{AP} \cos \alpha. \tag{6}$$

It is shown in the Appendix that there is no contribution to interfacial distortions beyond that generated by the homogeneous shear strain from either

Fig. 4

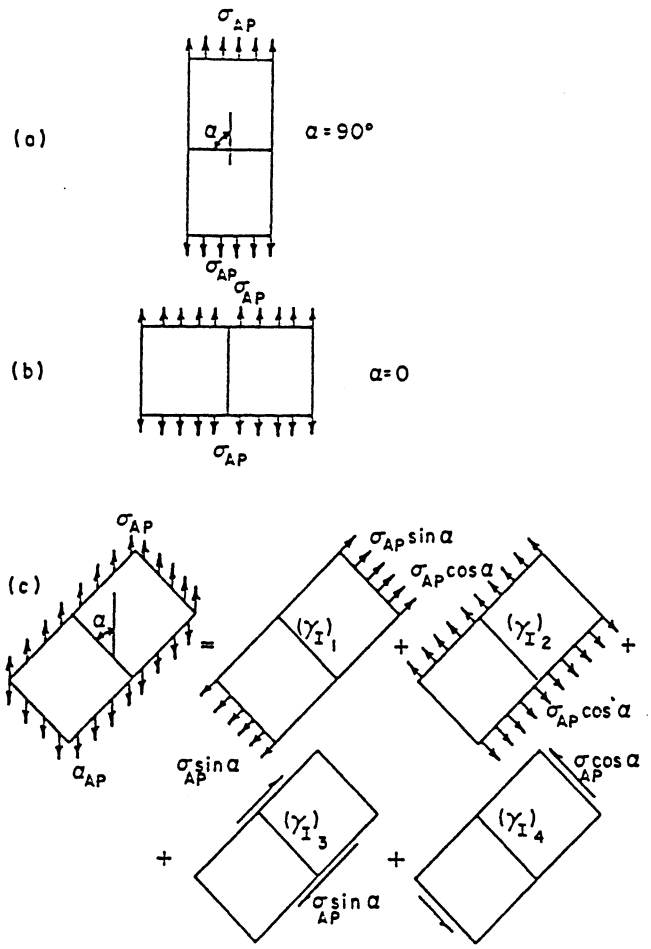

Three orientations of stress axis with respect to grains. (*a*) Stress axis perpendicular to interface plane ($\alpha = 90°$); (*b*) stress axis parallel to interface plane ($\alpha = 0$); (*c*) stress axis inclined to interface plane and decomposition of stress state into four different stress configurations by the application of the principle of superposition.

$(\gamma_I)_3$ or $(\gamma_I)_4$. They can be assumed to be zero, since they correspond to the homogeneous shear strains acting on the whole body. Substituting eqns. (5) and (6) into eqn. (4) gives

$$\gamma_I = \sigma_{AP}(k_1 \sin\alpha + k_2 \cos\alpha) \tag{7}$$

and, G being the shear modulus,

$$\tau_I = \sigma_{AP} G(k_1 \sin\alpha + k_2 \cos\alpha). \tag{8}$$

If one wishes to calculate the total stress, one has to add the term due to the homogeneous shear stress (eqn. (2)):

$$\tau_T = \sigma_{AP} G(k_1 \sin\alpha + k_2 \cos\alpha) + \frac{\sigma_{AP}}{2} \sin 2\alpha. \tag{9}$$

Applying the constants from the table to the finite-element analysis of the Appendix, one finds that $k_1 = 3 \times 10^{-12}$ Pa^{-1} and $k_2 = 12 \times 10^{-12}$ Pa^{-1} for nickel. The grain with the highest shear modulus is the one under highest interfacial shear stress. Taking the [111] grain, one finds, substituting the values into eqn. (8),

$$\frac{\tau_I}{\sigma_{AP}} = 115 \times 10^{-3}(3 \sin \alpha + 12 \cos \alpha). \tag{10}$$

The maximum value of the interfacial stress/applied ratio occurs for $\alpha = 0$ (geometry shown in fig. 4) :

$$\frac{\tau_I}{\sigma_{AP}} = 1{\cdot}37. \tag{11}$$

Hence, the interfacial shear stress is three times higher than the resolved shear stress homogeneously applied on the grain ($\tau_H = \sigma_{AP}/2$).

2.3. *Shear incompatibility*

Figure 5 shows the elastic shear strains undergone by two adjacent cubes when stressed under tension. In the reference system shown, one has

$$\gamma_{13} = \tan \theta_s \quad \text{or} \quad \gamma_{12} = \tan \theta_s. \tag{12}$$

In order to determine θ_s and, consequently, γ_{13} and the interfacial shear stresses due to elastic shear incompatibility, an approach different from that of § 2.2 has to be used ; the finite-element method cannot be used here because the program only operates for isotropic materials, which do not exhibit shear strains in the reference system defined by the tensile axis. Hence, a combination of tensor treatment of the cubic elastic constants and of the methods of ' mechanics of materials ' will be used.

The case to be analysed is a crystal with [110] aligned with the tensile axis. Other directions also result in shear strains γ_{13}, but it suffices to provide a preliminary estimate. The two [110] crystals in fig. 5 are oriented in such a way that the shear strains take place along opposite directions ; if they occurred in the same direction, the deformation would be compatible. The transformation of axes shown in the right-hand-side of fig. 5 (*a*) is performed in order to find the components of the cubic elastic compliance matrix in the new system (45° rotation around Ox_3). From

$$S'_{ijkl} = l_{im} l_{jn} l_{ko} l_{lp} S_{mnop},$$

$$\frac{S'_{16}}{2} = S'_{1112} = l_{11}l_{11}l_{11}l_{21}S_{11} + l_{12}l_{12}l_{12}l_{22}S_{22} + l_{11}l_{12}l_{11}l_{22}\frac{S_{66}}{4} + l_{11}l_{11}l_{12}l_{22}S_{12}, \tag{13}$$

$$S'_{16} = \frac{S_{44}}{8} + \frac{S_{12}}{2}, \tag{14}$$

where l_{ij} are the direction cosines of the new coordinate system and S_{ijkl} and S_{mn} are the compliances in the tensor and matrix notation, respectively. Applying values from the table for nickel, one obtains

$$S'_{16} = -0{\cdot}035 \times 10^{-11} \text{ Pa}^{-1}.$$

Fig. 5

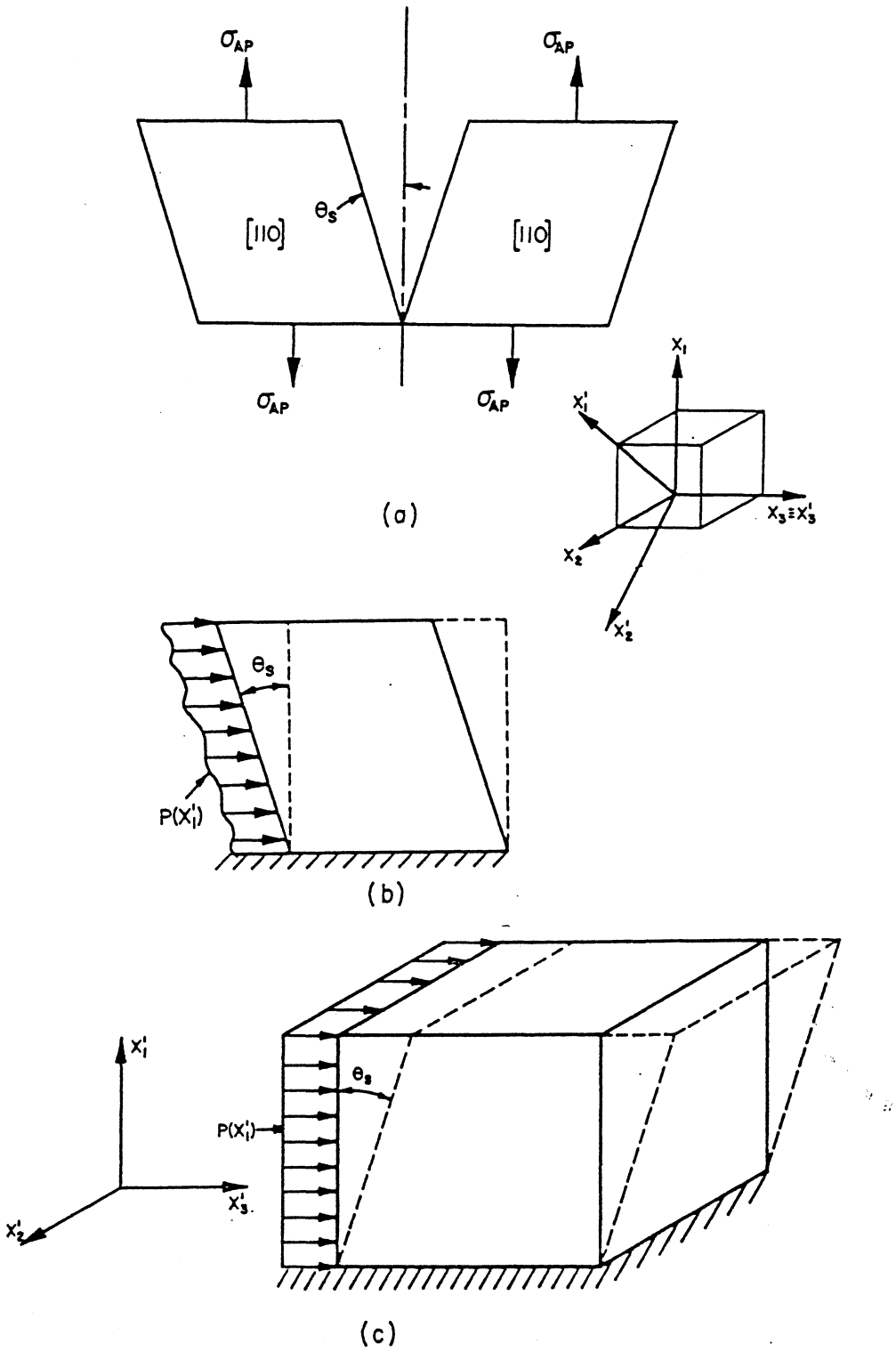

(*a*) Shear incompatibility when two grains having the [110] along the tensile axis, but having the other directions making 180° are stressed in tension. (*b*) Grain viewed as a beam that is loaded by $P(x'_1)$ until the faces regain normality. (*c*) Reverse (but identical) situation to (*b*), in which an initially cubic beam is sheared by angle θ on application of distributed load $P(x'_1)$.

The applied stress is σ'_{11} ; hence, one has :

$$\epsilon'_{12}=S'_{1211}\,\sigma'_{11}=\frac{S'_{16}}{2}\,\sigma'_{11}=0{\cdot}0175\times10^{-11}\sigma'_{11}. \tag{15}$$

On the other hand, one finds that $S'_{15}=0$ and, consequently, $\epsilon'_{13}=0$. In order to determine the stress at the interfacial layer due to the distortion θ_s, it is helpful to re-propose the problem as shown in fig. 5 (*b*) : a distributed load $P(x'_1)$ required to produce a shear θ_s in a beam which is placed on a fixed support (cross-hatched in fig. 5 (*b*)). One now has to revert to an isotropic material (with elastic constants E and G). Figure 5 (*c*) shows the inverse problem, whose solution should be the same ; a short beam on a fixed support is sheared by a distributed load to an angle θ_s. (The solution to this problem is given by Higdon, Ohlsen, Stiles, Weese and Riley (1976).) The deflection of the beam is produced by the bending moment and shear stresses. For long, slender beams the bending-moment effect is dominant, while in short, heavily loaded beams the deflection produced by shearing stresses is significant. The beam in fig. 5 (*c*) has a square cross-sectional area, and the length L is equal to the thickness D. Assuming a uniformly distributed load for simplicity (per unit length of beam), one has the following expression for the total deflection (eqn. (*a*) in § 6–12 of Higdon *et al.* 1976) :

$$x'_1=\frac{3wL^4}{2EAD^2}+\frac{3wL^2}{4AG}. \tag{16}$$

But $D=L$ and $A=L^2$, so

$$x'_1=\frac{3w}{2E}+\frac{3w}{4G}=3w\left(\frac{1}{2E}+\frac{1}{4G}\right). \tag{17}$$

The deflection θ_s is small, in such a way that

$$\tan\theta_s=\frac{x'_1}{D}=\gamma_s=2\epsilon'_{12}. \tag{18}$$

Substituting eqn. (18) into eqn. (17), one arrives at

$$3w=\frac{D\tan\theta_s}{(1/2E)+(1/4G)}. \tag{19}$$

From eqn. (15),

$$w=\frac{0{\cdot}012\times10^{-11}\sigma'_{11}\,D}{(1/2E)+(1/4G)}. \tag{20}$$

The load per unit beam thickness is, actually, the stress. This interfacial stress, σ_I, is

$$\sigma_I=\frac{0{\cdot}012\times10^{-11}\sigma_{AP}}{(1/2E)+(1/4G)}. \tag{21}$$

One can compute it for nickel by applying the values of E and G taken from the table (taking the value of E for [110] and computing G therefrom) and calculating the interfacial shear stresses :

$$\tau_I=0{\cdot}012\sigma_{AP}. \tag{22}$$

This value is very low, in comparison with the elastic longitudinal incompatibility stresses (eqn. (11)). Hence, one can neglect the elastic shear incompatibility stresses.

§ 3. Plastic incompatibility

3.1. *Microyielding in grain boundaries*

The actual shear stress at the grain boundaries significantly exceeds the homogeneous shear stress; the situation is depicted schematically in fig. 1 (*a*). Hence, yielding starts along the grain boundaries. Grain boundaries have been known to be sources of dislocations; Li (1963) and Price and Hirth (1972) have proposed specific mechanisms. When the stress reaches the critical level required for emission, localized plastic deformation will start. These dislocations do not propagate throughout the grain for two reasons:

(1) the stress decreases rapidly with distance from the grain boundary, and

(2) the centre of the grains is under the control of the homogeneous shear stress, which is a maximum at 45° to the tensile axis. On the other hand, the interfacial and homogeneous shear stresses have different orientations. Figure 6 shows how the dislocations emitted from the grain boundaries will undergo cross-slip. Extensive cross-slip and the generation of dislocation locks will result in a localized layer with high dislocation density.

Fig. 6

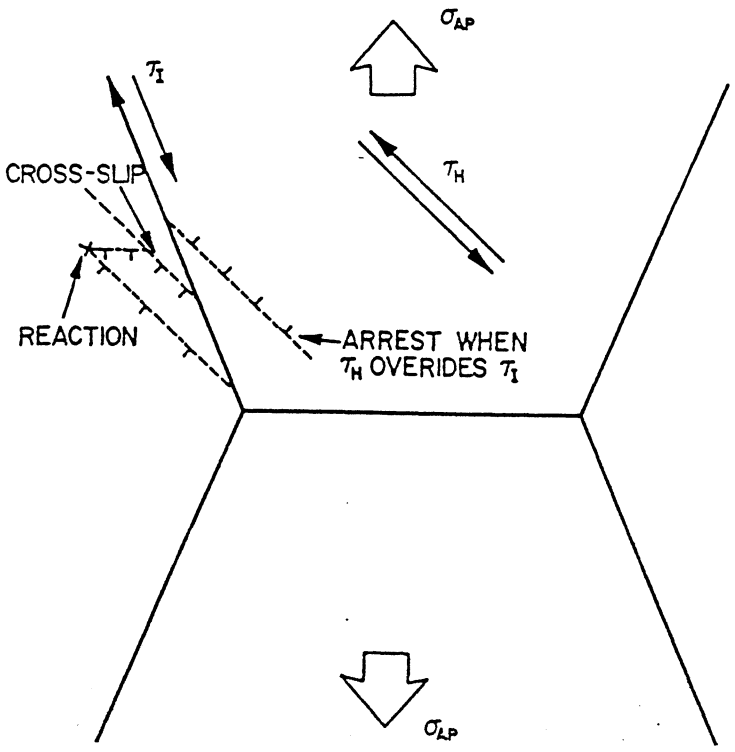

Dislocation arrest, cross-slip and reactions as they pass from the region of dominance of τ_I to the region of dominance of τ_H.

These dislocations generated at the interfaces can be classified as 'geometrically necessary' (Ashby 1970). Their introduction will accommodate the two adjacent grains, decreasing the incompatibility stresses. Figure 1 (*b*) shows the levelling off of the stresses ; as the applied stress increases, the ratio between interfacial and applied stress (eqn. (10)) decreases. The stresses become homogeneous when the interfacial layer is completed (fig. 1 (*c*)). This marks the onset of the dominance of plastic incompatibility.

The microstructure shown in fig. 1 (*c*) is composed of a continuous network of grain-boundary material with flow stress σ_{fGB} and discontinuous pockets of bulk material with flow stress σ_{fB}. Here σ_{fB} can be considered as the yield stress of monocrystalline material when oriented for multiple slip, while σ_{fGB} is the flow stress of the work-hardened grain-boundary layer. Hence, one can consider the material as a composite ; the yield stress of composite materials is treated in detail by Kelly (1971). Models have been developed taking into account the morphology, connectivity and plastic constants of the different components ; for the purpose of the model presented here, the simplest situation will be analysed (§ 3.2). One can see intuitively that the fraction of grain-boundary material increases as the yield stress of the composite increases.

3.2. *Mathematical analysis*

In the most simple case in which reinforcing fibres are continuous and parallel to the tensile axis, and neglecting differences in elastic constants between the matrix and fibres, it is customary to apply the simple 'law of mixtures' to predict the yield stress of the composite :

$$\sigma_c = V_f\sigma_{ff} + V_m\sigma_{fm}. \tag{23}$$

Here, σ_c, σ_{ff} and σ_{fm} are the flow stresses of the composite, fibre and matrix, respectively ; V_f and V_m are their volume fractions. Indeed, Margolin and Stanescu (1975) apply this equation. In the case of continuous fibres the volume fraction of fibres is equal to the area fraction along a normal cross-sectional area. It is this latter parameter that is of importance, because it determines the load-bearing partitioning among the two components of the composites. For the case under investigation, a continuous network of grain-boundary material with thickness t in a material with grain size D, one does not have the equality above. Hence, a more correct formulation is :

$$\sigma_y = A_B\sigma_{fB} + A_{GB}\sigma_{fGB}, \tag{24}$$

where A_{GB} and A_B are the area fractions of the grain-boundary network and of the bulk pockets. For simplicity, it will be assumed that both adjacent grains and grain-boundary regions have the same elastic moduli ; this is different from the assumptions made in § 2. The new assumptions are justified by the fact that one is now in the region of plastic incompatibility. Equation (24) expresses the fact that the polycrystalline 'composite' will yield plastically when the stress at the grain-boundary layers reaches a critical level equal to σ_{fGB}. Plastic flow in the interior of the grains is inhibited, when $\sigma_{AP} > \sigma_{fB}$, by the continuous network of grain-boundary material. If the network were discontinuous, one could not use eqn. (24).

From eqn. (24) one can obtain an expression relating the yield stress and grain size. Depending on the simplifying assumptions, different expressions

Fig. 7

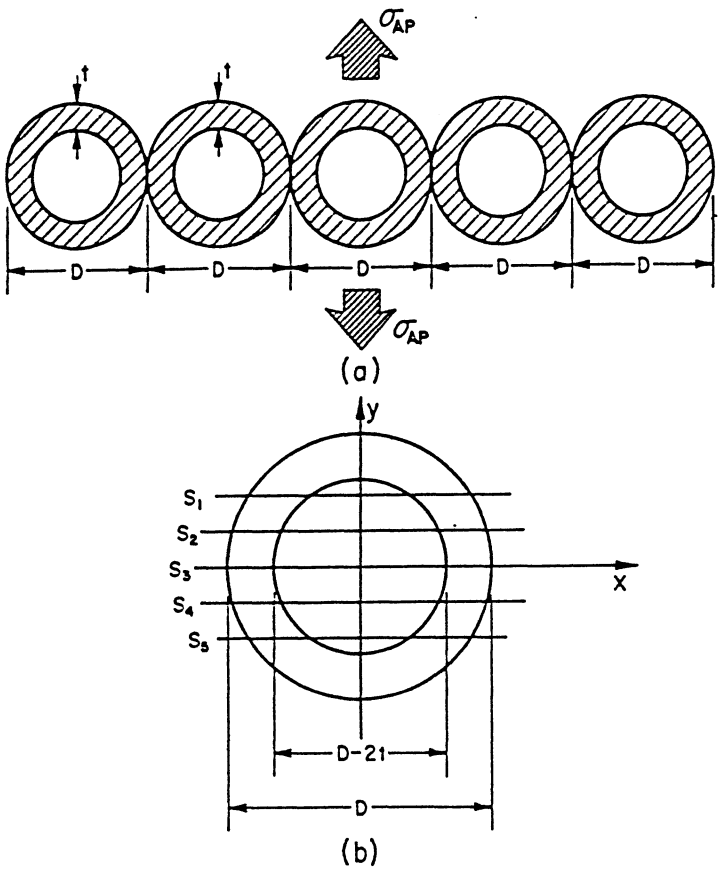

(*a*) Polycrystalline aggregate viewed as composite material composed of bulk and grain-boundary material, with flow stresses σ_{fB} and σ_{fGB} respectively. (*b*) Idealized spherical grain of diameter D with grain-boundary layer of thickness t; sections S_1, S_2, S_3, S_4 and S_5 reveal different proportions between the areas of the bulk and grain-boundary material.

are obtained. Two derivations will be presented. The first is based on the sketch shown in fig. 7 (*a*). The grains are assumed to be spheres with diameter D and with a grain-boundary layer of thickness t. A diametric cross-section will establish the area fractions

$$A_{GB} = \frac{\frac{1}{4}\pi[D^2 - (D-2t)^2]}{\frac{1}{4}\pi D^2}, \tag{25}$$

$$A_B = \frac{\frac{1}{4}\pi(D-2t)^2}{\frac{1}{4}\pi D^2}. \tag{26}$$

Substituting eqns. (25) and (26) into eqns. (24) gives

$$\sigma_y = \sigma_{fB} + 4(\sigma_{fGB} - \sigma_{fB})tD^{-1} - 4(\sigma_{fGB} - \sigma_{fB})t^2D^{-2}. \tag{27}$$

Equation (27) predicts, as expected that $\sigma_y = \sigma_{fB}$ for very large values of D, and $\sigma_y = \sigma_{fGB}$ when $D = 2t$ (the whole of the material is grain-boundary layer).

A second equation can be obtained by making slightly more sophisticated assumptions. If one takes a section through a material composed of quasi-spherical gains with equal diameter, the intersections will not all be diametric. Figure 7 (*b*) shows how this affects the average apparent diameter. The sections S_1, S_2, S_3, S_4 and S_5 yield different values for the diameter and different widths of the work-hardened layer. If this correction is introduced, the average diametric section is :

$$\bar{D}=\frac{\int_0^{D/2}(D^2/4-y^2)^{1/2}\,dy}{\int_0^{D/2}dy}=\frac{\pi}{4}D. \tag{28}$$

The average thickness is obtained likewise, as

$$\bar{t}=\frac{D-2t}{D}\frac{\int_0^{(D-2t)/2}\{(D^2/4-y^2)^{1/2}-[((D-2t)/2)^2-y^2]^{1/2}\}\,dy}{\int_0^{(D-2t)/2}dy}+\frac{2t}{D}\frac{\int_{(D-2t)/2}^{D/2}(D^2/4-y^2)^{1/2}dy}{\int_{(D-2t)/2}^{D/2}dy}. \tag{29}$$

One finds that $\bar{t}\sim 1{\cdot}8t$ for t substantially smaller than D. When $t=D/2$, one has the same relationship as eqn. (28). Margolin and Stanescu (1975) used the expression below :

$$\bar{t}=1{\cdot}57t. \tag{30}$$

Calculating the average bulk and grain-boundary area fractions per cross-section assuming a mean diameter $\bar{D}$ and a mean grain-boundary thickness $\bar{t}$, one obtains

$$\sigma_y=\sigma_{iB}+4(\sigma_{iGB}-\sigma_{iB})\bar{t}\bar{D}^{-1}-4(\sigma_{iGB}-\sigma_{iB})\bar{t}^2\bar{D}^2. \tag{31}$$

Substituting eqns. (28) and (30) into eqn. (31), one arrives at

$$\sigma_y=\sigma_{iB}+8(\sigma_{iGB}-\sigma_{iB})tD^{-1}-16(\sigma_{iGB}-\sigma_{iB})t^2D^{-2}. \tag{32}$$

If one assumes a constant t, eqn. (32) is approximately a D^{-1} relationship. The D^{-2} term is unimportant for large grain sizes (D^{-2} much smaller than D^{-1}). When the grain size decreases, the negative D^{-2} term becomes more important, ' bending down ' the curve so that it approaches σ_{iGB} (when $t=D/2$). On the other hand, different dependencies can be obtained by considering a variable t. One way of obtaining the classical $D^{-1/2}$ dependence for values of D greater than $2t$ is to assume that

$$t=kD^{1/2}. \tag{32 a}$$

Physically, the meaning of eqn. (32 *a*) is that, at small grain sizes, t increases rapidly with grain diameter ; at large grain sizes the dependence is smaller. Substituting eqn. (32 *a*) into eqn. (32), one obtains

$$\sigma_y=\sigma_{iB}+8k(\sigma_{iGB}-\sigma_{iB})D^{-1/2}-16k^2(\sigma_{iGB}-\sigma_{iB})D^{-1}. \tag{33}$$

Equation (33) predicts a $D^{-1/2}$ relationship at large grain sizes, when the $D^{-1/2}$ term predominates. As the grain size decreases, the D^{-1} term becomes more important, 'bending down' the curve until it flattens out at $t \simeq D/2$, for a stress $\sigma_y = \sigma_{IGB}$.

§ 4. Comparison with experiments

The experimental results obtained by Thompson (1975, 1977), Anderson *et al.* (1968) and Abrahamson (1968) over a wide range of grain sizes provide the verification for the model proposed in this paper. The results obtained by Thompson, especially, show that large deviations from a Hall–Petch relationship are obtained at very small grain sizes. Figure 8 shows the results obtained by Thompson (1977) for nickel. It can be seen that the Hall–Petch relationship is not obeyed for grain sizes below 1 μm ; there is a yield-stress plateau. Equations (27), (32) and (33), the three formulations of the model, are also plotted in fig. 8. The value $\sigma_{iB} = 20$ MPa, $\sigma_{iGB} = 280$ MPa and $t = 0{\cdot}2$ μm were used. The choice of these values is justified by the general morphology of the plot of σ_y versus $D^{-1/2}$. The flow stress of a monocrystal oriented for polyslip, corrected by the Taylor factor ($M = 3{\cdot}06$) was found to be close to 20 MPa (Thompson 1977). The yield stress seems to saturate around 280 MPa, so this is thought to be a reasonable value for σ_{iGB}. For eqns. (27) and (32), t was assumed to be constant ; since the change of regime takes place for a grain size of about 0·4 μm ($D^{-1/2} \sim 1{\cdot}5$ $\mu m^{-1/2}$), a grain-boundary thickness of 0·2 μm was thought to be reasonable. It should be noticed that no adjustable parameter, other than the appropriate choice of σ_{iB}, σ_{iGB} and t, was used in eqns. (27) and (32).

Equation (33), on the other hand, contains a parameter k which was not available ; assuming a best fit for the curve in the Hall–Petch range (cross-hatched in fig. 7), a slope of 260 was found. From this a value of 0·125

Fig. 8

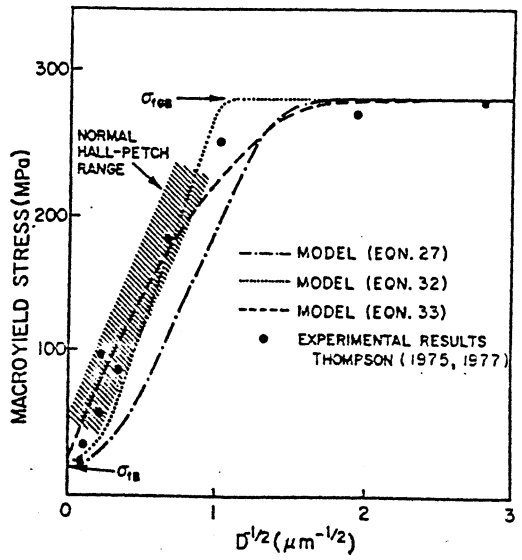

Comparison of model with results obtained by Thompson (1975, 1977) for nickel.

$(260 \times 8 \times k)$ was obtained from eqn. (33). Equation (33) has the advantage of predicting a $D^{-1/2}$ relationship for the larger grain sizes; as the grain size is decreased beyond a certain value the negative term (increasing in magnitude with D^{-1}) becomes more and more important. This curve approaches the $\sigma = 280$ MPa line asymptotically because the thickness of the grain-boundary layer decreases as the grain size is decreased. Of the three formulations, eqn. (33) seems to provide the best fit with the experimental results obtained by Thompson (1977).

§ 5. Conclusions

(1) A model for the effect of grain size on the yield stress of metals is proposed. The model rests on the following sequence of microdeformation processes. (*a*) Elastic incompatibility stresses at the grain boundaries are produced by the elastic anisotropy of crystal. (*b*) These elastic anisotropy stresses, added to the uniformly distributed stress (resolved shear stress due to applied load), exceed the flow stress of the grain boundary before the polycrystalline aggregate, as a whole, is able to deform plastically. (*c*) A work-hardened layer of grain-boundary material is formed in a continuous network pattern, relieving the elastic incompatibility stresses. (*d*) At this point, the polycrystalline aggregate is effectively a composite material composed of a continuous network of interfacial material ($\sigma_{f(GB)}$) and discontinuous 'islands' of bulk material ($\sigma_{fB} < \sigma_{f(GB)}$).

(2) The model is expressed quantitatively as three equations relating the macroyield stress to grain size, and resting on some slightly different hypotheses. Two equations, based on a constant thickness of the grain-boundary layer, lead to a D^{-1} relationship for large grain sizes. The third, based on $t \propto D^{1/2}$, leads to the classical Hall–Petch relationship ($D^{-1/2}$) for large grain sizes.

(3) The model is compared with experimental results reported by Thompson (1977) over a wide range of grain sizes for nickel.

Acknowledgments

We wish to thank Professors J. R. C. Guimarães and R. N. Orava for thoughtfol comments on earlier versions of this manuscript, and Professor H. Margolin for having provided preprints. This research was partially supported by the Research and Developement Division of the New Mexico Institute of Mining and Technology, Research Division of the South Dakota School of Mines and Technology, and by National Science Foundation Grant DMR-797102.

APPENDIX

The finite-element analysis

The determination of the stress and strain distributions along the grain boundary is beyond the possibilities of an analytical solution; hence, it is necessary to employ a numerical model. Finite-element analsyis was chosen,

a simple two-dimensional plane strain/plane stress constant strain-triangle computer code being utilized. The finite-element method has found a wide application in a variety of structural engineering problems. The method subdivides the continuum into a mesh of elements of finite sizes; triangular elements are the simplest. The continuum mechanics equations for continuity and equilibrium are replaced by matrix equations involving 'equivalent' loads on each element, the displacement of each node or corner of the element, and the 'stiffness' of the total system. The matrix equations are solved for the unknown nodal displacements by large-matrix inversion techniques. Stresses in each element are then calculated from the corresponding nodal displacements. The stresses and displacements calculated by the method are approximate and their accuracy depends on the sophistication of the mesh and type of finite element used. The computer program used is a modification of the program given by Desai and Abel (1972). Margolin and co-workers (Margolin and Stanescu 1975, Jinoch *et al.* 1978, Ankem and Margolin 1980) have used similar codes to treat micromechanical problems.

Figure 9 shows the mesh used in the present analysis. Elements 1 to 40 belong to the first grain; elements 41 to 80 belong to the second grain; the grid has an axis of symmetry, shown in fig. 9. Accordingly, the elements in which the interfacial shear strains are greatest are elements 5 and 80;

Fig. 9

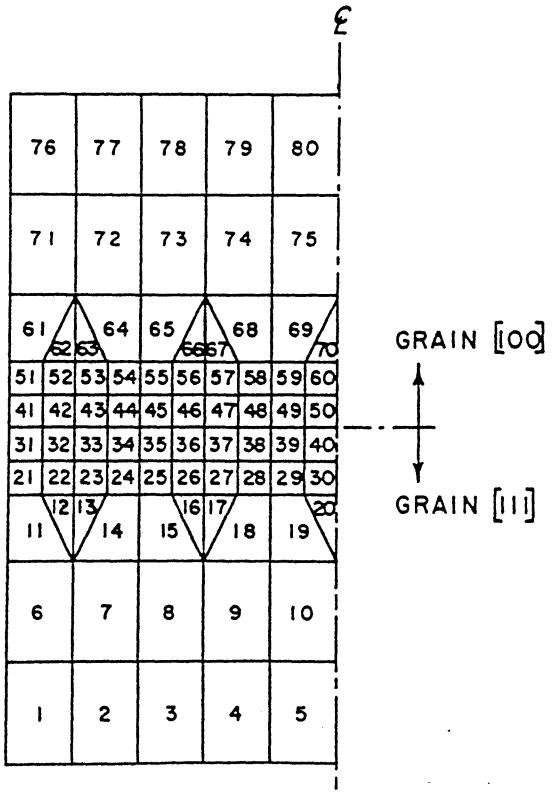

Finite element mesh used to simulate the grains. Mesh size is reduced close to interface. Note axis of symmetry.

hence, they are lowest at elements 40 and 50. The elements are smaller close to the interface to allow for larger changes in strain. In its present form, the number of elements of the program is limited to approximately 100. The program can be applied to only two stress states : plane stress or plane strain. The state of stress that more closely resembles the one encountered in the uniform extension of the grains is a uniaxial stress state. Both plane-stress and plane-strain configurations were used ; however, all the results reported are for a plane-strain configuration (the third dimension of the cube is assumed to be infinite), and consequently an error is inevitably introduced. The stresses and displacements at the centre of the elements are calculated ; one of the nodes is fixed so that its displacement is set equal to zero. Figures 10, 11 and 12 show the displacements for three different configurations of applied

Fig. 10

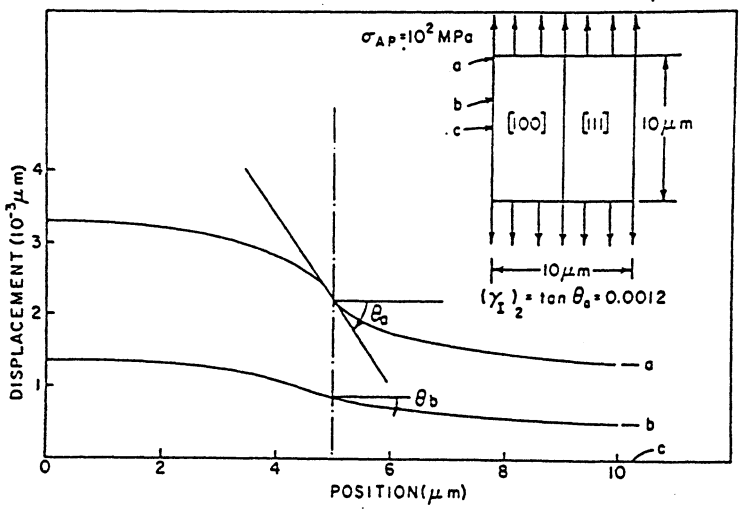

Displacement fields for configuration giving $(\gamma_I)_2$. $D=10\ \mu m$; $\sigma_{AP}=10^2$ MPa.

Fig. 11

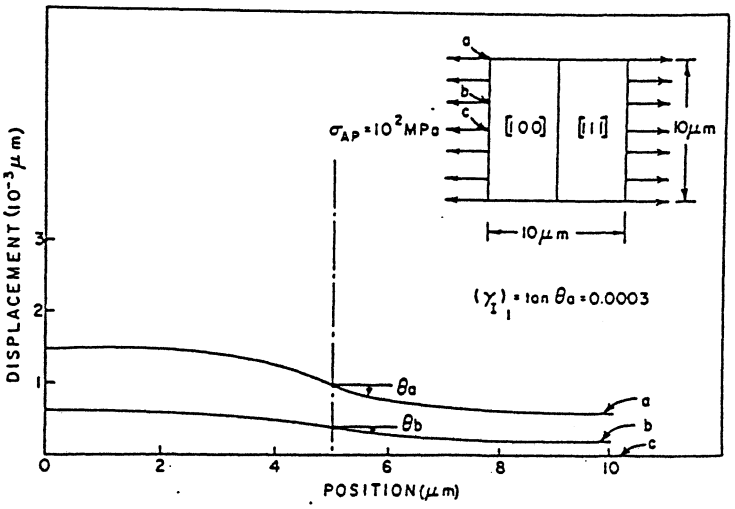

Displacement fields for configuration giving $(\gamma_I)_1$. $D=10\ \mu m$; $\sigma_{AP}=10^2$ MPa.

Fig. 12

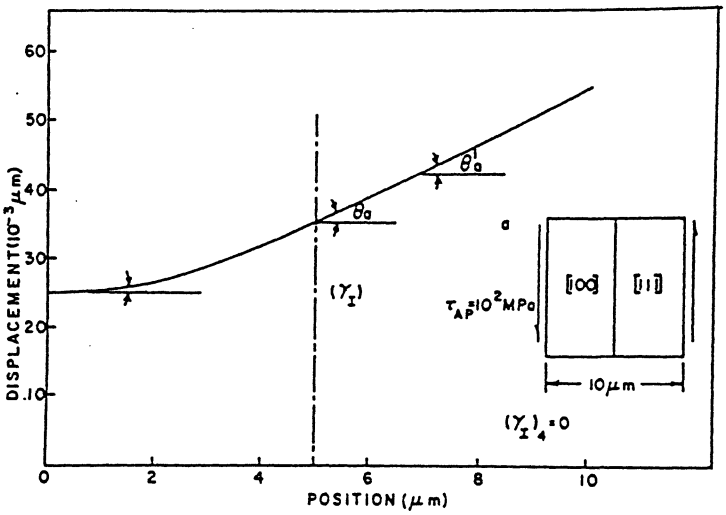

Displacement fields for configuration giving $(\gamma_I)_4$. $D = 10\ \mu m$; $\sigma_{AP} = 10^2$ MPa.

stress. They are obtained by varying the orientation of the surface tractions acting on the grid of fig. 9. The applied stress is 10^2 MPa and the grid (grain) size is about 10 μm for the three configurations. These configurations correspond to the orientations needed to calculate the interfacial strains of fig. 4 (*c*). The computer-generated displacements were plotted at three positions (*a*, *b* and *c* in figs. 10 and 11). It can be seen that the interfacial shear strain, given by the tangent of the angle θ at the interface, is the greatest for *a* and zero for *c*. This is expected, because the distortions should be zero at the central plane (because of the symmetry) and increase as the distance from it increases, and confirms the schematic indication of fig. 3. The interfacial strains $(\gamma_I)_2$ (fig. 10), $(\gamma_I)_1$ (fig. 11) and $(\gamma_I)_4$ (fig. 12) are calculated by taking the tangent of

Fig. 13

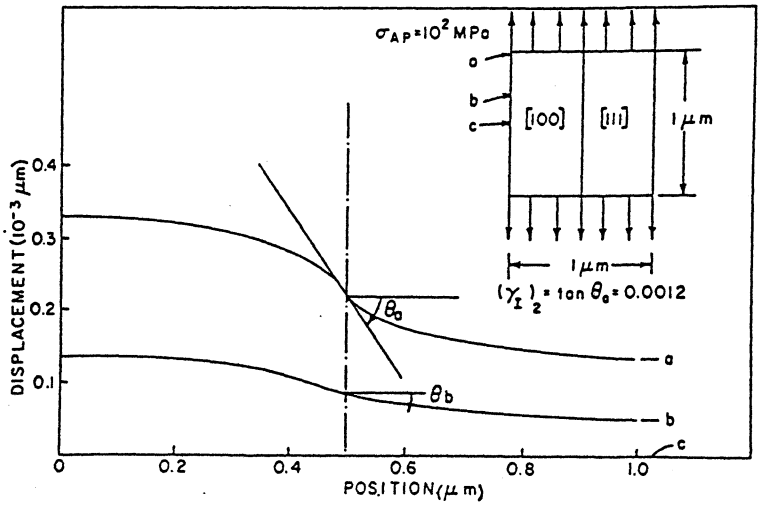

Displacement fields for configuration giving $(\gamma_I)_2$. $D = 1\ \mu m$; $\sigma_{AP} = 10^2$ MPa.

Fig. 14

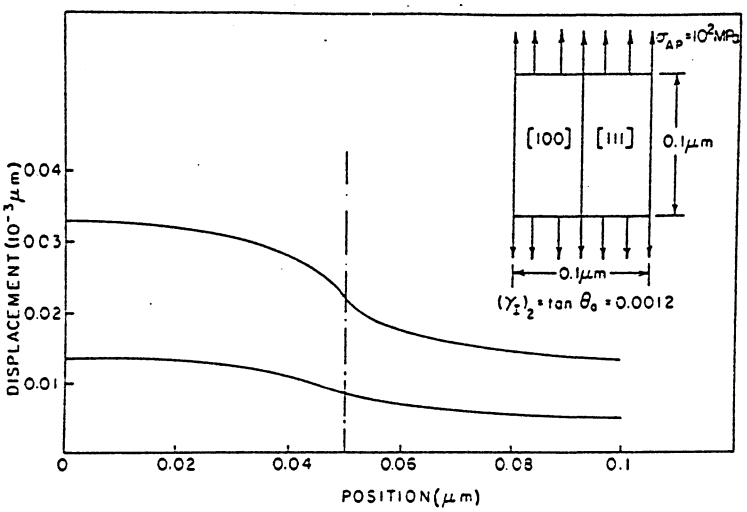

Displacement fields for configuration giving $(\gamma_I)_2$. $D=0{\cdot}1$ μm ; $\sigma_{AP}=10^2$ MPa.

the maximum distortion θ (at a). It can be readily seen that $(\gamma_I)_2$ is substantially larger than $(\gamma_I)_1$ for the given cube size and at the applied level : $(\gamma_I)_2 \simeq 4(\gamma_I)_1$. The ratio should be fairly independent of cube size and stress level. There is no *per se* contribution to interfacial strain from the configuration of fig. 12 because the displacement fields do not exhibit an inflection point at the interface. The angle θ_a at the interface has essentially the same value as that at a region removed from it in grain [111] (θ'_a). Hence, the displacement shown represents the homogeneous contribution to shear ; the configuration providing $(\gamma_I)_3$ was not analysed by the finite-element method, because it is essentially identical to the one providing $(\gamma_I)_4$; if one is operating under conditions in which the strain tensor is symmetric ($\gamma_{23}=\gamma_{32}$ in fig. 4 (*c*)), one should not expect any contribution to the interfacial strain from it.

The effect of grain size on the displacement fields was assessed by decreasing the grain size of the configuration of fig. 10 to 1 and 0·1 μm. The resultant displacement fields are shown in figs. 13 and 14 respectively. It is immediately seen that the displacements are exactly scaled down in the same proportion, resulting in no change in $(\gamma_I)_2$. The result is really significant and indicates that no change in interfacial stress concentration should be expected if the material responds as modelled in the previous analysis. The grain boundary is a region in which the atoms are relaxed from their original lattice positions ; solute atoms are often attracted to the grain boundary, resulting in segregation. There are other situations in which the solute atoms are repelled from it, causing denudation. These compositional changes reflect themselves in changes in the elastic constants. An attempt was made to assess the effect of the interfacial layer on the stress level at the grain boundary. There are at least two parameters : Young's modulus and thickness. By taking an interfacial layer with a thickness of 0·2 μm and assuming its Young's modulus to be 80 GPa, the results presented in fig. 15 were obtained. The effect of grain size is clearly seen. The finite-element mesh had to be modified to allow

Fig. 15

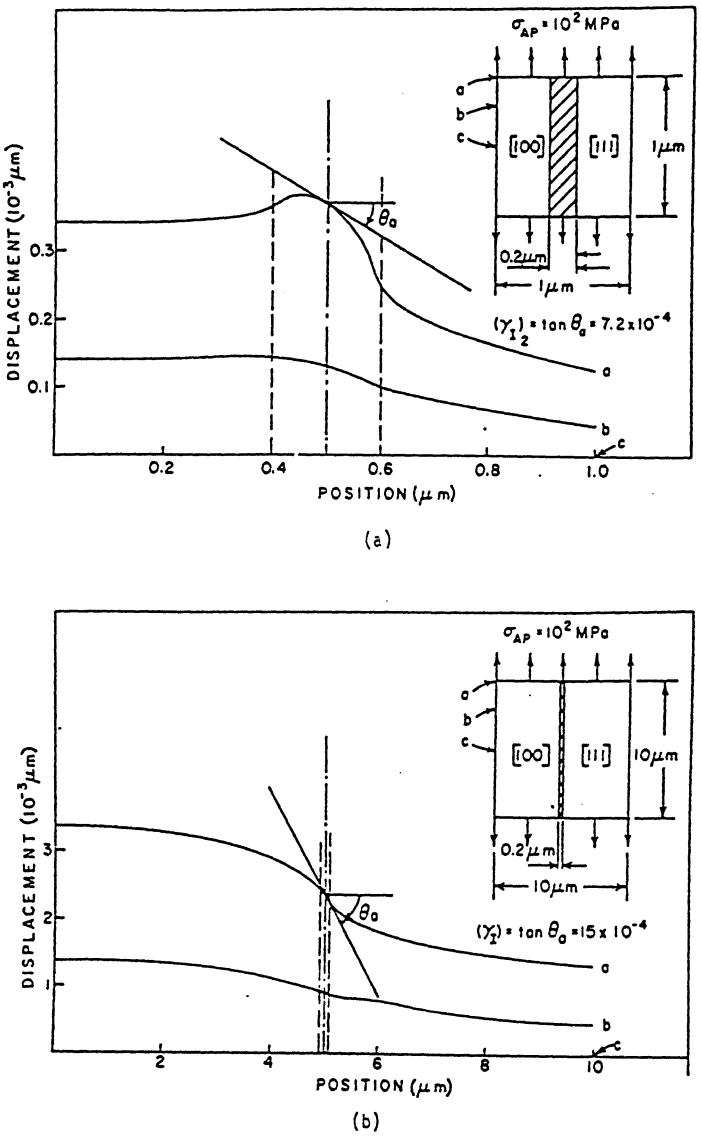

Displacement fields for configuration giving $(\gamma_I)_2$ with a 0·2 μm grain-boundary layer ($\sigma_{AP} = 10^2$ MPa). (*a*) $D = 1$ μm ; (*b*) $D = 10$ μm.

this interfacial layer to be introduced. From a comparison of figs. 15 (*a*) and 15 (*b*), it can be seen that $(\gamma_I)_2$ is substantially lower for the 1 μm than for the 10 μm grain size. Thus, one can conclude that grain-boundary segregation and denudation might have an effect on the incompatibility stresses, and consequently on the grain-size dependence of the yield stress.

References

Abrahamson, E. P., II, 1968, *Surfaces and Interfaces II* (Syracuse University Press), p. 262.

Anderson, E., King, D. W., and Spreadborough, J., 1968, *Trans. metall. Soc. A.I.M.E.*, 242, 115.

ANKEM, S., and MARGOLIN, H., 1980, Report N-00014-75-C-0793, Office of Naval Research.
ASHBY, M. F., 1970, *Phil. Mag.*, **21**, 399; 1971, *Strengthening Methods in Crystals*, edited by A. Kelly and R. B. Nicholson (New York: Wiley), p. 137.
BALDWIN, W. M., JR., 1958, *Acta metall.*, **6**, 89.
BISHOP, J. F., and HILL, R., 1951, *Phil. Mag.*, **41**, 1298.
BRENTNALL, W. D., and ROSTOKER, W., 1965, *Acta metall.*, **13**, 187.
CONRAD, H., 1963, *Acta metall.*, **11**, 75.
COTTRELL, A. H., 1958, *Trans. metall. Soc. A.I.M.E.*, **212**, 192.
DESAI, C. S., and ABEL, J. F., 1972, *Introduction to the Finite Element Method* (New York: Van Nostrand), p. 439.
DOUTHWAITE, R. M., and EVANS, J. T., 1973, *Acta metall.*, **21**, 525.
HALL, E. O., 1951, *Proc. R. Soc.* B, **64**, 474.
HIGDON, A., OHLSEN, E. H., STILES, W. B., WEESE, J. A., and RILEY, W. R., 1976, *Mechanics of Materials*, third edition (New York: John Wiley), p. 406.
HIRTH, J. P., 1972, *Metall. Trans.*, **3**, 3047.
HOOK, R. E., and HIRTH, J. P., 1967, *Acta metall.*, **15**, 535, 1099.
HULL, D., 1961, *Acta metall.*, **9**, 191.
JINOCH, J., ANKEM, S., and MARGOLIN, H., 1978, *Mater. Sci. Engng.*, **34**, 203.
KELLY, A., 1971, *Strengthening Methods in Crystals*, edited by A. Kelly and R. B. Nicholson (New York: John Wiley), p. 433.
LI, J. C. M., 1962, *Direct Observation of Imperfections in Crystals*, edited by J. B. Newkirk and E. Wernick (New York: Interscience), p. 234; 1963 a, *J. Aust. Inst. Metals*, **8**, 206, 381; 1963 b, *Trans. metall. Soc. A.I.M.E.*, **227**, 239.
LI, J. C. M., and CHOU, Y. T., 1970, *Metall. Trans.*, **1**, 1145.
MCGREGOR TEGART, M. J., 1966, *Elements of Mechanical Metallurgy* (New York: MacMillan), pp. 89, 91.
MARCINKOWSKI, M. J., and LIPSITT, H. A., 1962, *Acta metall.*, **10**, 95.
MARGOLIN, H., and STANESCU, M. S., 1975, *Acta metall.*, **23**, 1411.
MOTT, N. F., 1946, *J. Inst. Metals*, **72**, 367.
MURR, L. E., 1975, *Metall. Trans.* A, **6**, 427.
MURR, L. E., and HECKER, S. S., 1979, *Scripta metall.*, **13**, 167.
NYE, J. F., 1957, *Physical Properties of Crystals* (Oxford University Press), pp. 134, 145.
PETCH, N. J., 1953, *J. Iron Steel Inst.*, **174**, 25.
PRICE, C. W., and HIRTH, J. P., 1972, *Mater. Sci. Engng.*, **9**, 15.
SETHI, V. K., and GIBALA, R., 1976, *Thin Solid Films*, **39**, 79; 1977, *Acta metall.*, **25**, 321.
SMITH, C. S., 1952, *Metal Interfaces* (Metals Park, Ohio, American Society for Metals), p. 65.
SUITS, J. C., and CHALMERS, B., 1961, *Acta metall.*, **9**, 854.
TALIA, J. E., FERNANDEZ, L., SETHI, V. K., and GIBALA, R., 1980, *Strength of Metals and Alloys*, edited by P. Haasen, V. Gerold and G. Kostorz (Toronto: Pergamon Press), p. 127.
TANGRI, K., and MALIS, T., 1972, *Surf. Sci.*, **31**, 101.
TAYLOR, G. I., 1938, *J. Inst. Metals*, **62**, 307.
THOMPSON, A. W., 1975, *Acta metall.*, **23**, 1337; 1977, *Ibid.*, **25**, 83.
THOMPSON, A. W., BASKES, M. I., and FLANAGAN, W. F., 1973, *Acta metall.*, **21**, 1017.
WORTHINGTON, P. J.. and SMITH, E., 1964, *Acta metall.*, **12**, 1277.